Magnetic excitations in the topological semimetal $YbMnSb_2$

Siobhan M. Tobin,[1,*] Jian-Rui Soh,[2] Hao Su,[3] Andrea Piovano,[4] Anne Stunault,[4] J. Alberto Rodríguez-Velamazán,[4] Yanfeng Guo,[3,5] and Andrew T. Boothroyd[1,†]

[1]*Department of Physics, University of Oxford, Clarendon Laboratory, Oxford OX1 3PU, United Kingdom*
[2]*Institute of Physics, Ecole Polytechnique Fédérale de Lausanne (EPFL), CH-1015 Lausanne, Switzerland*
[3]*School of Physical Science and Technology, ShanghaiTech University, Shanghai 201210, China*
[4]*Institut Laue-Langevin, 6 rue Jules Horowitz, Boîte Postale 156, 38042 Grenoble Cedex 9, France*
[5]*ShanghaiTech Laboratory for Topological Physics, ShanghaiTech University, Shanghai 201210, China*

(Received 15 February 2023; revised 27 April 2023; accepted 28 April 2023; published 23 May 2023)

We report neutron scattering measurements on $YbMnSb_2$ which shed light on the nature of the magnetic moments and their interaction with Dirac fermions. Using half-polarized neutron diffraction we measured the field-induced magnetization distribution in the paramagnetic phase and found that the magnetic moments are well localized on the Mn atoms. Using triple-axis neutron scattering we measured the magnon spectrum throughout the Brillouin zone in the antiferromagnetically ordered phase, and we determined the dominant exchange interactions from linear spin-wave theory. The analysis shows that the interlayer exchange is five times larger than in several related compounds containing Bi instead of Sb. We argue that the coupling between the Mn local magnetic moments and the topological band states is more important in $YbMnSb_2$ than in the Bi compounds.

DOI: 10.1103/PhysRevB.107.195146

I. INTRODUCTION

Topological metals and semimetals have excellent transport qualities as a result of special geometrical properties of the quasiparticles associated with linear electronic band crossings near to the Fermi energy. Magnetism can dramatically influence topological electronic states, and offers the possibility of using magnetic fields to manipulate the attendant physical characteristics [1,2]. How magnetic order couples to the topological quasiparticles is an interesting and multifaceted question.

Thanks to ongoing developments in theory and experiment, the catalog of magnetic topological semimetals continues to expand. Several examples of such materials have been found among the $AMnX_2$ layered manganese pnictides (A = Ca, Sr, Ba, Yb, Eu; X = Bi, Sb) [2–21]. In this family, Dirac or Weyl fermions are harbored by the Bi or Sb square net, which lies between magnetic Mn layers. Although many $AMnX_2$ materials have closely related crystal structures, the Mn (and in some cases Eu) ions produce a variety of magnetic structures, which can be extended by the application of an external magnetic field.

In this work we shall focus on $YbMnSb_2$, which has been studied in detail via quantum oscillations, magnetometry, optical spectroscopy, *ab initio* band structure calculations, angle-resolved photoemission spectroscopy, and single-crystal neutron diffraction [18–21]. $YbMnSb_2$ is of particular note due to its superior thermoelectric properties among topological semimetals [22] as a result of anomalous transport in the Sb layer. The crystal structure of $YbMnSb_2$ is described by the $P4/nmm$ space group with lattice parameters $a = b = 4.31(2)$ Å, $c = 10.85(1)$ Å [20]. It orders antiferromagnetically below $T_N \approx 345$ K [18–21]. Several different magnetic structures were originally proposed based on *ab initio* calculations and experimental methods that indirectly probed the magnetic structure [18,19,21], but our recent neutron diffraction study [20] showed conclusively that the Mn spins order in a C-type antiferromagnetic (AFM) structure with spins along the c axis (the Yb atoms in $YbMnSb_2$ are nonmagnetic) (see Fig. 1).

Here we present the results from half-polarized neutron diffraction and unpolarized neutron inelastic scattering studies of $YbMnSb_2$. The former was designed to study how well the magnetic moments are localized on the Mn sites or elsewhere in the unit cell, while the latter was performed in order to measure the spin-wave spectrum. The overall aim was to determine the form and strength of the exchange interactions in $YbMnSb_2$ and to compare them with what has been found in a number of other isostructural $AMnX_2$ compounds. The interactions along the c axis are of particular interest as they are potentially mediated by topological relativistic fermions in Sb or Bi bands near the Fermi energy. We find that the spin-wave spectrum is well described by a Heisenberg effective spin-$\frac{1}{2}$ Hamiltonian with easy-axis anisotropy which has been used previously for $AMnX_2$. The in-plane exchange couplings are found to be similar to those in other $AMnX_2$ compounds, but the ferromagnetic (FM) exchange along

*siobhan.tobin@physics.ox.ac.uk
†a.boothroyd@physics.ox.ac.uk

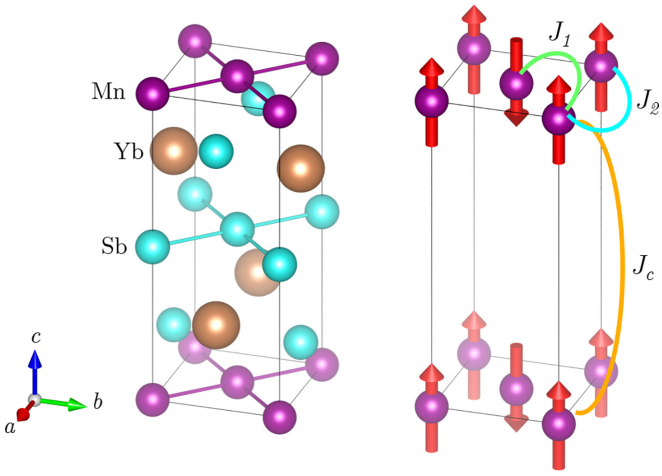

FIG. 1. Left: the unit cell of $YbMnSb_2$. Right: the same structural unit cell showing the observed *C*-type antiferromagnetic ordering of the Mn spins [20]. Magnetic moments indicated by red arrows, and exchange constants labeled as J_1 between *ab* plane nearest-neighbor Mn ions, J_2 between next-nearest-neighbor Mn ions and J_c along the *c* axis. Figure prepared using VESTA [23].

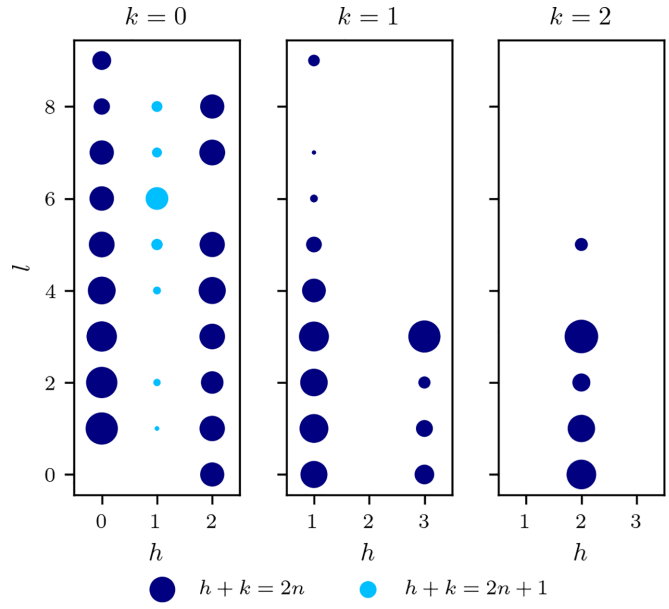

FIG. 2. Magnetic structure factors calculated from measured flipping ratios. The radius of the circles is proportional to the magnetic structure factor at that *hkl* reflection.

the *c* axis is five to six times larger. The results imply that the coupling between magnetism and relativistic fermions plays a more important role in $YbMnSb_2$ than in several related compounds containing Bi instead of Sb.

II. METHODS

Single crystals in the form of platelets of typical dimensions $4 \times 4 \times 0.2$ mm^3 were grown by a flux method, as detailed in [19,21]. For inelastic neutron scattering, 20 crystals with a total mass of 0.84 g were coaligned on a 0.5-mm-thick aluminum plate with the *c* axis perpendicular to the large face of the plate. Crystals were affixed with hydrogen-free CYTOP^{TM} fluoropolymer [24]. The quality of individual crystals as well as the overall coalignment of the crystals was checked using an x-ray Laue diffractometer (Photonic Science). The estimated mosaicity of the ensemble of crystals was $\sim 3^\circ$ (full width at half maximum) [25].

Half-polarized neutron diffraction was conducted on the D3 diffractometer at the Institut Laue-Langevin (ILL) [26]. A single crystal of $YbMnSb_2$ was prealigned using the ILL's neutron Laue diffractometer OrientExpress [27]. The crystal was oriented with the *b* axis perpendicular to the horizontal scattering plane. A vertical-field superconducting magnet provided a magnetic field of $\mu_0 H = 9.0$ T parallel to the *b* axis. Polarized neutrons of wavelength $\lambda = 0.832$ Å were produced by a Heusler monochromator, and a cryoflipper was used to switch their spin states from parallel to antiparallel with the external magnetic field. There was no polarization analysis of the scattered neutrons (half-polarized setup). Two erbium filters were placed in the incident beam to minimize $\lambda/2$ contamination. The sample was measured in the paramagnetic phase at a temperature of 400 K, with any ferromagnetism manifesting solely due to the applied magnetic field. Flipping ratios (i.e., the ratio of the diffracted intensities for neutrons with spins parallel and antiparallel to the applied field) were measured at a set of structural Bragg peaks and converted to field-induced magnetic structure factors by the standard method [28]. As the flipping ratios are all close to unity there is no ambiguity in the obtained magnetic structure factors. After averaging over symmetry-equivalent positions we obtained a total of 25 distinct magnetic structure factors at *h*0*l* reflections, as well as 20 out-of-plane reflections, *hkl* with $k = 1, 2$, that were accessible.

Inelastic neutron scattering was performed on the IN8 triple-axis spectrometer at the ILL with the FLATCONE multiplexed analyzer–detector system [29]. Measurements were taken at two different crystal orientations giving access to the (*h*0*l*) and (*hhl*) sections in reciprocal space, respectively. A fixed outgoing neutron wave vector of $k_f = 3$ Å^{-1} was selected by Bragg reflection from the silicon (Si) (111) analyzer crystals built into FLATCONE, and the incident wave vector k_i was varied to give a range of neutron energy transfers ΔE from 0 to 70 meV. Either a double-focusing Si(111) monochromator ($\Delta E < 40$ meV), or a double-focusing pyrolytic graphite (002) monochromator ($\Delta E \geqslant 40$ meV) was used to set k_i. The FLATCONE tilt was maintained at 0° throughout, and the sample was held at a temperature of 1.5 K in a liquid-helium "orange" cryostat.

III. RESULTS AND DISCUSSION

A. Half-polarized neutron diffraction

We first describe the results from the half-polarized neutron diffraction study. Figure 2 displays the positions in reciprocal space at which measurements were made, indicating the magnitude of the obtained field-induced magnetic structure factors F_M at each position, while Fig. 3 plots the F_M values with their experimental uncertainties as a function of the magnitude of the scattering vector $Q = |\mathbf{Q}|$. The majority of the measurements with nonzero F_M are at positions which satisfy $h + k = 2n$. This is the reflection condition for the

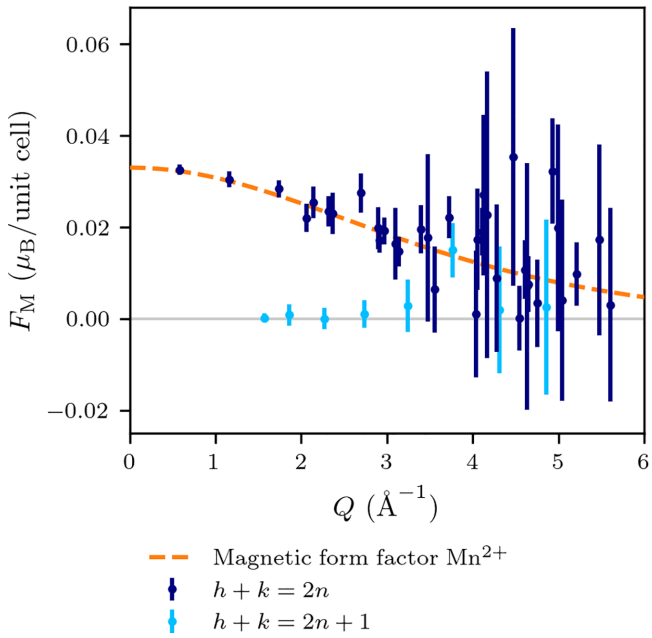

FIG. 3. Magnetic structure factors calculated from measured flipping ratios as a function of Q, compared to the calculated free-ion magnetic form factor of Mn^{2+}.

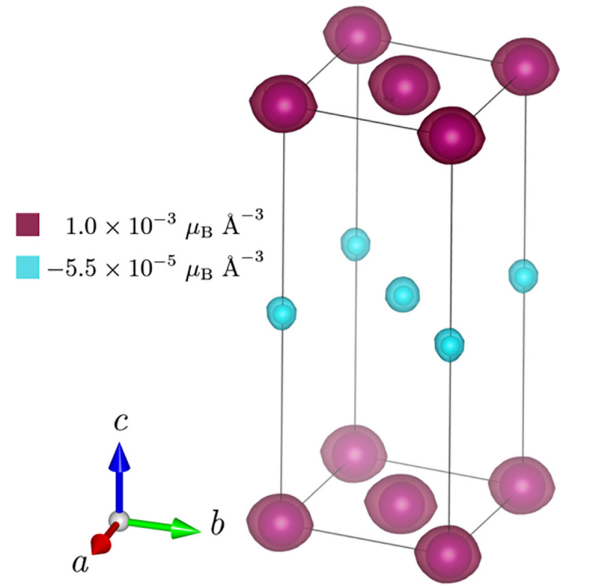

FIG. 4. Magnetization density distribution in the unit cell of $YbMnSb_2$, with isosurfaces showing strong concentration of magnetization on Mn sites and a very small negative magnetization on Sb sites in the middle of the unit cell.

lattice of Mn atoms which occupy Wyckoff site 2*a*, where most of the magnetization is expected to be centered, and also for the Sb atoms in site 2*b* located halfway between the Mn layers. We also included some reflections with $h = 1$, $k = 0$, $l \neq 0$ as a check. Nearly all of the F_M measured at these reflections, which are allowed by the space group $P4/nmm$ of the full crystal structure, are zero to within the experimental error, which indicates that there is very little magnetization associated with the Sb and Yb atoms located in the 2*c* Wyckoff sites. A model-free reconstruction of the magnetization distribution within the unit cell (Fig. 4) was obtained from the magnetic structure factors by the Bayesian maximum entropy (MaxEnt) method as implemented at the ILL, which incorporates routines from the MEMSYS subroutine library [30]. Cross sections through the reconstruction at fractional heights $z = 0$ and $z = 0.5$ are presented in Fig. 5, corresponding to the Mn layer and the central Sb layer. The magnetization maps show that the majority of the magnetism induced by the external field is localized around the Mn sites and is approximately isotropic, consistent with a roughly equal population of all five Mn 3*d* orbitals as expected for the high spin state of Mn^{2+} ($3d^5$, $S = 5/2$). By integrating a volume around the Mn site we find the total induced magnetic moment to be $0.011(4)\mu_B$ per Mn. A region of small negative magnetization is observed around the Sb sites in the central layer at $z = 0.5$, with the induced moment calculated to be $-0.0002(6)\mu_B$ per Sb. We used a method developed by Markvardsen to obtain these integrated moment values and their errors [31]. Although the MaxEnt method is designed to give a nonzero signal only when there is evidence for it in the data, the size of the uncertainty in the Sb moment is comparable with the moment itself, and so we are cautious about attributing statistical significance to this signal.

B. Triple-axis spectroscopy

Moving on to the magnetic excitations, we present our neutron spectroscopy data in Figs. 6–8. Figure 6 shows a series of constant-energy (ΔE) cuts parallel to the (00*l*), (*h*00), and (*hh*0) high-symmetry directions, and Figs. 7 and 8 show intensity maps recorded at different energies in the *h*0*l* and *hhl* reciprocal lattice planes, respectively. In the *h*0*l* plane, the intensity is localized around the magnetic Bragg peak positions at low energies. The intensity is highest at 10 meV, decreasing at lower energies until no signal is visible below about 5 meV (see Fig. 6, middle panels). Above 10 meV, the intensity disperses outwards with increasing energy to form rings which eventually merge into rods of scattering running along the (00*l*) direction. In the *hhl* plane, rods of scattering along (00*l*) are observed at all energies studied, with some intensity modulation along the rods at the lower energies. At higher energies the rods split into two, which then move apart. By 55 meV, the signal is almost unresolvable from the background. As we now show, the features just described are consistent with the scattering from spin-wave excitations of antiferromagnetically ordered Mn local moments.

In order to analyze the neutron inelastic scattering data [25], first, the NPLOT MATLAB scripts library [32] was used to smooth the background and manually remove spurions and powder rings.

Second, a suite of custom PYTHON programs (built using packages including those described in [33–35]) took care of visualization, interpolation, making one-dimensional cuts through the data along high-symmetry lines, and intensity peak fitting at different ΔE. Examples of constant energy cuts are shown in Fig. 6. The high-symmetry lines used for cuts were $\Lambda = (0, 0, l)$, $\Delta = (h, 0, 0)$, and $\Sigma = (h, h, 0)$. Additionally, the intensity maxima as a function of energy were found at the Γ and A points in order to anchor the turning

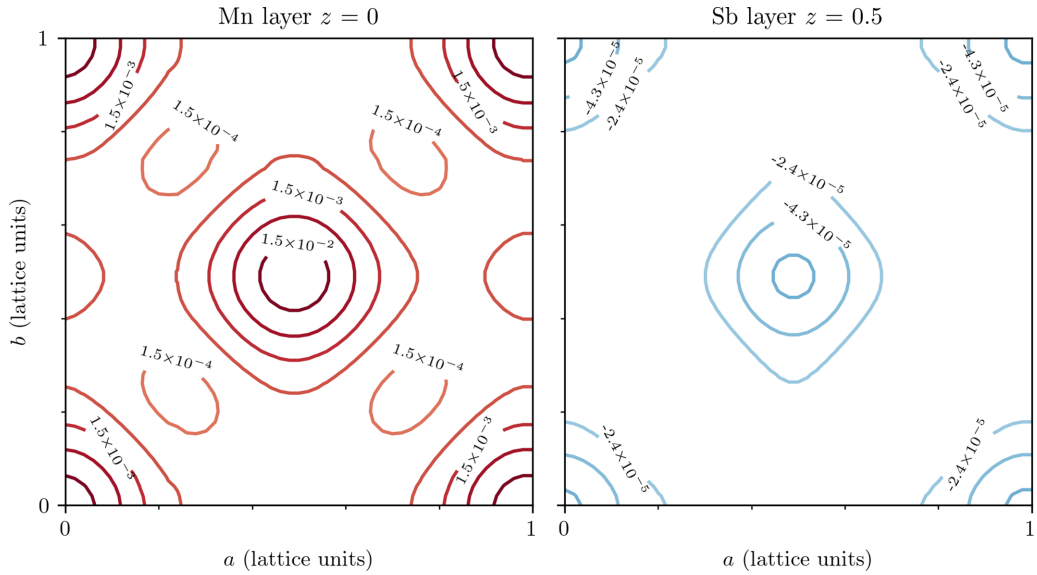

FIG. 5. Slices through the *ab* plane showing magnetization density map reconstructed from ILL D3 data. Contour lines show magnetization density in units of μ_B Å^{-3}.

points of the dispersion. Third, the extracted peaks were assembled into the spin-wave dispersion along high-symmetry paths in reciprocal space shown in Fig. 9.

Following the approach used in Refs. [6,36,37] for structurally related AMnX_2 compounds, we modeled the magnetic interactions in $YbMnSb_2$ with a Heisenberg effective spin Hamiltonian of the form

$$\mathcal{H} = \sum_{i,j} J_{ij} \mathbf{S}_i \cdot \mathbf{S}_j - \sum_i D\left(S_i^z\right)^2, \tag{1}$$

and calculated the spin-wave spectrum using linear spin-wave theory (LSWT) for spins $\mathbf{S}_i$ localized on the Mn ions. The parameters of $\mathcal{H}$ were obtained from a global fit to the measured dispersion curves using both custom PYTHON programs (orthogonal distance regression) and the SPINW MATLAB library [38]. Three isotropic exchange parameters, $J_{ij} = J_1$, J_2, and J_c as defined in Fig. 1, together with the single-ion anisotropy parameter D, which in Eq. (1) favors alignment of the Mn spins along the c axis, were found to be sufficient to obtain a good fit to the data.

The calculated LSWT dispersion obtained from the best-fit parameters is shown in Fig. 9 along with the data points. Overall, there is a good match between the model and the data along all high-symmetry directions. The fitted model indicates that the spin-wave dispersion has a maximum energy of approximately 70 meV which occurs at the X point in the Brillouin zone, where $X = (\frac{1}{2}, 0, 0)$, and a minimum gap of about 10 meV at the Γ point.

A more complete comparison of the measured and calculated spin-wave spectrum can be made by inspection of Figs. 7 and 8. The bottom rows of panels show simulations of the LSWT spectrum in the same region of reciprocal space and for the same energies as probed experimentally. The magnetic form factor of Mn^{2+} is included in the simulations. It can be seen that the model reproduces the distribution of measured intensity throughout energy and momentum space very well.

The Hamiltonian parameters extracted from the LSWT fit are $SJ_1 = 28 \pm 2$ meV, $SJ_2 = 10.4(5)$ meV, $SJ_c = -0.73(7)$ meV, and $SD = 0.44(5)$ meV (the spin quantum number S always multiplies the Hamiltonian parameters in LSWT). Here, positive values represent antiferromagnetic coupling, while negative values imply ferromagnetic coupling. The larger uncertainty in the SJ_1 value may be attributed to the inherent broadening of the dispersion in the *ab* plane, caused by the imperfect coalignment of the platelet crystals in this plane. According to the convention in Eq. (1), the positive value of SD means that the Mn spins preferentially align along the c axis, as observed experimentally [20]. The exchange constants are presented in Table I.

For comparison, we have also included in Table I the experimentally determined structural and exchange parameters for several other materials closely related to $YbMnSb_2$. There are a number of interesting points to note from the data. First, the T_N of $YbMnSb_2$ is distinctly higher than that of the other materials, hinting at a more robust magnetically ordered phase with stronger interactions. The exchange constants we have obtained reinforce this, with SJ_1, SJ_2, and SJ_c all greater for $YbMnSb_2$ than for other materials in the AMnX_2 family, especially SJ_c. Second, the a lattice parameter of $YbMnSb_2$ is about 5% smaller than that of the other materials, which likely explains why the SJ_1 and SJ_2 parameters are largest for $YbMnSb_2$. Third, the Mn-X-Mn bond angles associated with the the J_1 and J_2 superexchange paths both increase slightly, from 65.92° to 67.10° for J_1 and 100.60° to 102.82° for J_2, going from $YbMnBi_2$ to $YbMnSb_2$. These changes will tend to reduce the AFM superexchange contribution to J_1 and increase it for J_2, consistent with what is observed, although the effect is smaller than the overall increase in J_1 and J_2 associated with the decrease in a.

Finally, and perhaps most interesting, the distance between Mn atoms in the c direction is almost the same for all the compounds listed in Table I, and yet SJ_c is around five times

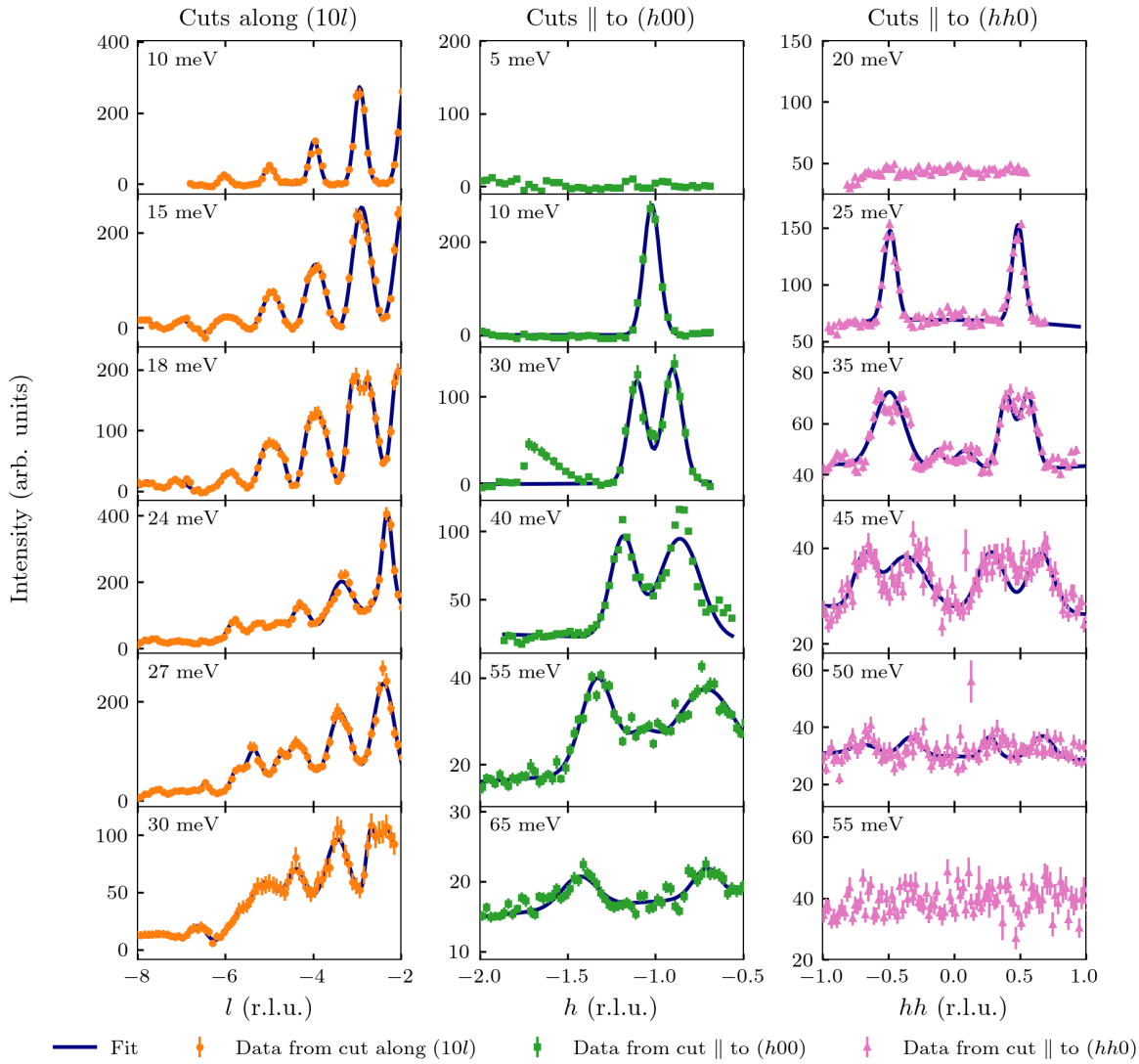

FIG. 6. Examples of one-dimensional, constant-energy cuts along high-symmetry directions. The (10l) cuts and cuts parallel to (h00) were from the $h0l$ plane dataset, while the cuts parallel to (hh0) were from the hhl dataset. At different energies, the cuts parallel to (h00) and (hh0) were performed at different integer l values as the detector coverage of reciprocal space varied. At energies >40 meV, the spin-wave intensity is low, so the cuts were averaged over a range of l values to improve the statistics. The lines are fits to the data to determine the magnon dispersion from the peak positions. A line shape comprising one or more Gaussian peaks and a linear background was used.

TABLE I. Experimentally determined parameters for $AMnX_2$. Exchange constants J_1, J_2, and J_c are defined in Fig. 1, and D is the easy-axis anisotropy parameter. Mn-X-Mn bond angles: angle 1 is with one Mn located at the corner of the unit cell and the other in the center of the $z = 0$ face, and angle 2 is with the Mn located on neighboring corners of the unit cell. Values in parentheses are errors in the last digits.

Material	Space group	a (Å)	c (Å)	T_N (K)	SJ_1 (meV)	SJ_2 (meV)	SJ_c (meV)	SD (meV)	Mn-X-Mn bond angle 1 (deg)	Mn-X-Mn bond angle 2 (deg)
$CaMnBi_2$ [6]	$P4/nmm$	4.50	11.07	264	23.4(6)	7.9(5)	−0.10(5)	0.18(3)	67.219(2)	103.04(1)
$SrMnBi_2$ [6]	$I4/nmm$	4.58	23.14	287	21.3(2)	6.39(15)	0.11(2)	0.31(2)	68.047(1)	104.614(1)
$YbMnBi_2$ [36]	$P4/nmm$	4.49	10.86	290	22.6(5)	7.8(5)	−0.13(5)	0.37(4)	65.92(4)	100.60(7)
$YbMnBi_2$ [37][a]	$P4/nmm$	4.48	10.8	290	22.7(3)	7.8(2)	−0.16(3)	0.43(4)		
$YbMnSb_2$ (this work and [20])	$P4/nmm$	4.31(2)	10.85(1)	345	28 ± 2	10.4(5)	−0.73(7)	0.44(5)	67.10(4)	102.82(7)

[a]The quoted parameters are from an analysis method which is similar to that used to obtain the other parameters listed in this table. A resolution-corrected fitting method gave the following parameters: $SJ_1 = 25.9(2)$ meV, $SJ_2 = 10.1(3)$ meV, $SJ_c = -0.130(3)$ meV, and $SD = 0.20(1)$ meV.

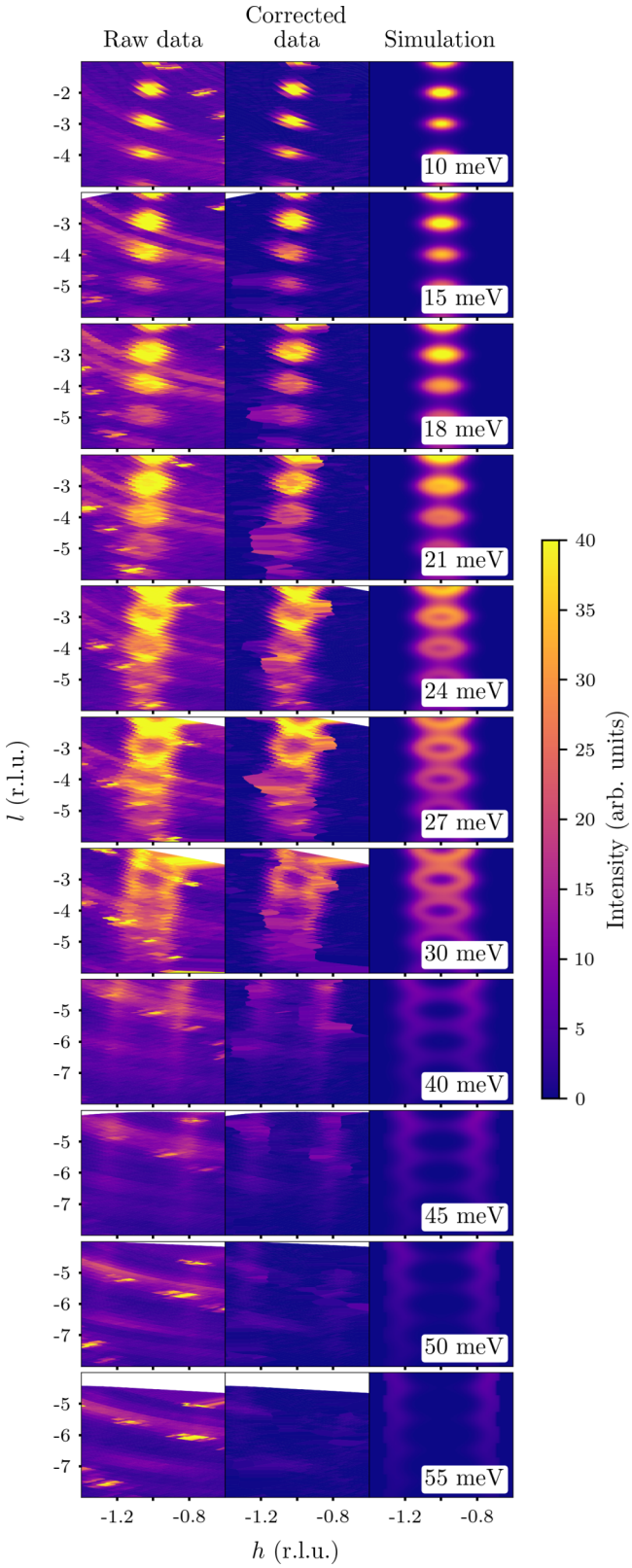

FIG. 7. Spin-wave scattering and model for *h*0*l* plane. Left column: raw neutron scattering data. Middle column: data after the corrections described in the text. Right column: magnetic scattering simulated by linear spin-wave theory from our model.

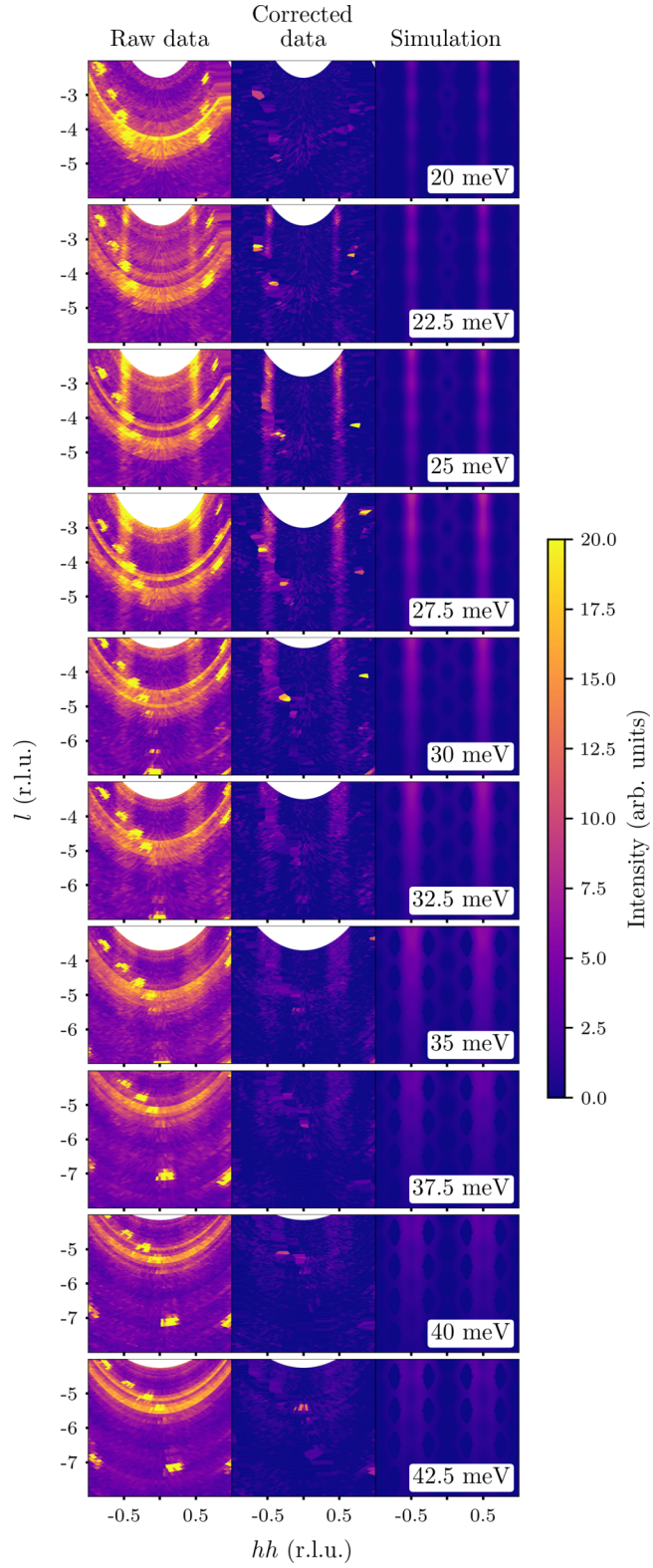

FIG. 8. Spin-wave scattering and model for the *hhl* plane. Left column: raw neutron scattering data. Middle column: data after the corrections described in the text. Right column: magnetic scattering simulated by linear spin-wave theory from our model.

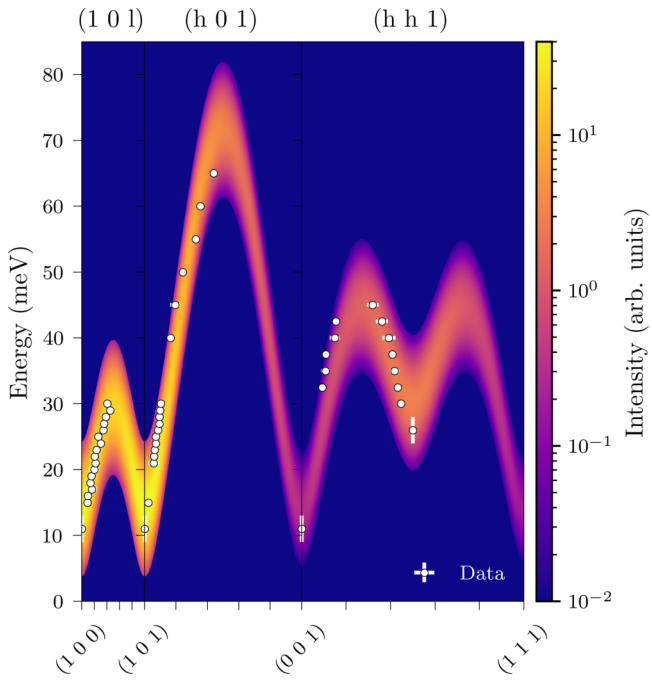

FIG. 9. Spin-wave dispersion of $YbMnSb_2$. The data points are shown as white circles, and the spin-wave spectrum calculated from our model is shown as an intensity map with a logarithmic color scale. The simulation includes a Gaussian energy broadening of 8 meV (FWHM).

larger in $YbMnSb_2$ than in the Bi compounds. This suggests that J_c is not affected so much by differences in the exchange path geometry, but rather by the fact that the p orbitals that mediate superexchange are lower in energy in Sb than in Bi. Assuming that J_c is determined by a competition between FM metallic double exchange and AFM superexchange [10], we expect a weaker AFM superexchange and hence a stronger net FM J_c in Sb relative to Bi, as observed. This implies that coupling between magnetism and the relativistic fermions that occupy the Dirac-like pnictogen bands located near the Fermi level may play a more important role in $YbMnSb_2$ than in the Bi compounds.

IV. CONCLUSION

Our experiments have shown that the magnetic moments in $YbMnSb_2$ are well localized on the Mn atoms, and so a semiclassical spin-wave description of the magnetic dynamics in the antiferromagnetically ordered phase is appropriate.

The exchange interactions determined in this work from the magnon dispersion of $YbMnSb_2$ are all larger than in several related compounds containing Bi instead of Sb which have been studied recently. The value of the interlayer coupling J_c is particularly notable, being around five times larger in $YbMnSb_2$ than in the Bi compounds. Considering the different superexchange and metallic contributions to J_c, we argue that the coupling between Dirac fermions and local spin moments on Mn may be more prominent in $YbMnSb_2$ than in the related Bi compounds. This suggests that $YbMnSb_2$ is a promising system with which to investigate the interplay between magnetism and topological band electrons.

Note added. Recently, a related study appeared in which the spin dynamics in $YbMnSb_2$ was measured by time-of-flight inelastic neutron scattering [39]. The spin Hamiltonian parameters obtained in that work are broadly in agreement with ours. The authors of Ref. [39] also present data on the damping of the spin-wave modes.

Data from the neutron experiments are available from the ILL via proposals No. 4-01-1684 (IN8 [40]) and No. 5-53-305 (D3 [41]).

ACKNOWLEDGMENTS

We thank Igor Mazin for insights on the exchange interactions, and all those involved in the ILL VISA project that made it possible to perform the neutron scattering experiments remotely during the coronavirus pandemic in 2020-2021. We also benefited from the ILL crystal alignment and structural characterization instruments CYCLOPS (experiment No. EASY-671) and Orient Express (experiment No. EASY-667). Y.F.G. and A.T.B. acknowledge support from the Oxford–ShanghaiTech collaboration project. Y.F.G. was supported by the Double First-Class Initiative Fund of ShanghaiTech University. S.M.T. was supported by a scholarship from the Rhodes Trust. J.-R.S. acknowledges support from the Singapore National Science Scholarship, Agency for Science Technology and Research, and also from the European Research Council under the European Union's Horizon 2020 research and innovation program synergy grant (HERO, Grant No. 810451).

[1] A. A. Burkov, Topological semimetals, Nat. Mater. **15**, 1145 (2016).
[2] S. Klemenz, S. Lei, and L. M. Schoop, Topological semimetals in square-net materials, Annu. Rev. Mater. Res. **49**, 185 (2019).
[3] D. Gong, S. Huang, F. Ye, X. Gui, J. Zhang, W. Xie, and R. Jin, Canted Eu magnetic structure in $EuMnSb_2$, Phys. Rev. B **101**, 224422 (2020).
[4] J.-R. Soh, P. Manuel, N. M. B. Schröter, C. J. Yi, F. Orlandi, Y. G. Shi, D. Prabhakaran, and A. T. Boothroyd, Magnetic and electronic structure of Dirac semimetal candidate $EuMnSb_2$, Phys. Rev. B **100**, 174406 (2019).
[5] Q. Zhang, J. Liu, H. Cao, A. Phelan, D. Graf, J. F. DiTusa, D. A. Tennant, and Z. Mao, Toward tunable quantum transport and novel magnetic states in $Eu_{1-x}Sr_xMn_{1-z}Sb_2$ ($z < 0.05$), NPG Asia Mater. **14**, 22 (2022).
[6] M. C. Rahn, A. J. Princep, A. Piovano, J. Kulda, Y. F. Guo, Y. G. Shi, and A. T. Boothroyd, Spin dynamics in the antiferromagnetic phases of the Dirac metals $AMnBi_2$ (A = Sr, Ca), Phys. Rev. B **95**, 134405 (2017).
[7] S. Borisenko, D. Evtushinsky, Q. Gibson, A. Yaresko, K. Koepernik, T. Kim, M. Ali, J. van den Brink, M. Hoesch, A. Fedorov, E. Haubold, Y. Kushnirenko, I. Soldatov, R. Schäfer,

and R. J. Cava, Time-reversal symmetry breaking type-II Weyl state in $YbMnBi_2$, Nat. Commun. **10**, 3424 (2019).

[8] J. B. He, Y. Fu, L. X. Zhao, H. Liang, D. Chen, Y. M. Leng, X. M. Wang, J. Li, S. Zhang, M. Q. Xue, C. H. Li, P. Zhang, Z. A. Ren, and G. F. Chen, Quasi-two-dimensional massless Dirac fermions in $CaMnSb_2$, Phys. Rev. B **95**, 045128 (2017).

[9] K. Wang, D. Graf, L. Wang, H. Lei, S. W. Tozer, and C. Petrovic, Two-dimensional Dirac fermions and quantum magnetoresistance in $CaMnBi_2$, Phys. Rev. B **85**, 041101(R) (2012).

[10] Y. F. Guo, A. J. Princep, X. Zhang, P. Manuel, D. Khalyavin, I. I. Mazin, Y. G. Shi, and A. T. Boothroyd, Coupling of magnetic order to planar Bi electrons in the anisotropic Dirac metals $AMnBi_2$ (A = Sr, Ca), Phys. Rev. B **90**, 075120 (2014).

[11] Z. Zhang, Z. Guo, J. Lin, F. Sun, X. Han, G. Wang, and W. Yuan, Effect of Cu doping on structure and physical properties in the antiferromagnetic Dirac semimetal $CaMnBi_2$, Inorg. Chem. **61**, 4592 (2022).

[12] J. Liu, J. Hu, H. Cao, Y. Zhu, A. Chuang, D. Graf, D. J. Adams, S. M. A. Radmanesh, L. Spinu, I. Chiorescu, and Z. Mao, Nearly massless Dirac fermions hosted by Sb square net in $BaMnSb_2$, Sci. Rep. **6**, 30525 (2016).

[13] K. Wang, D. Graf, H. Lei, S. W. Tozer, and C. Petrovic, Quantum transport of two-dimensional Dirac fermions in $SrMnBi_2$, Phys. Rev. B **84**, 220401(R) (2011).

[14] J. Y. Liu, J. Hu, Q. Zhang, D. Graf, H. B. Cao, S. M. A. Radmanesh, D. J. Adams, Y. L. Zhu, G. F. Cheng, X. Liu, W. A. Phelan, J. Wei, M. Jaime, F. Balakirev, D. A. Tennant, J. F. DiTusa, I. Chiorescu, L. Spinu, and Z. Q. Mao, A magnetic topological semimetal $Sr_{1-y}Mn_{1-z}Sb_2$ (y, $z < 0.1$), Nat. Mater. **16**, 905 (2017).

[15] A. Wang, I. Zaliznyak, W. Ren, L. Wu, D. Graf, V. O. Garlea, J. B. Warren, E. Bozin, Y. Zhu, and C. Petrovic, Magnetotransport study of Dirac fermions in $YbMnBi_2$ antiferromagnet, Phys. Rev. B **94**, 165161 (2016).

[16] X.-S. Ni, C.-Q. Chen, D.-X. Yao, and Y. Hou, Origin of the type-II Weyl state in topological antiferromagnetic $YbMnBi_2$, Phys. Rev. B **105**, 134406 (2022).

[17] A. Pal, M. Chinotti, L. Degiorgi, W. Ren, and C. Petrovic, Optical properties of $YbMnBi_2$: A Type II Weyl semimetal candidate, Phys. B: Condens. Matter **536**, 64 (2018).

[18] R. Kealhofer, S. Jang, S. M. Griffin, C. John, K. A. Benavides, S. Doyle, T. Helm, P. J. W. Moll, J. B. Neaton, J. Y. Chan, J. D. Denlinger, and J. G. Analytis, Observation of a two-dimensional Fermi surface and Dirac dispersion in $YbMnSb_2$, Phys. Rev. B **97**, 045109 (2018).

[19] Z. Qiu, C. Le, Z. Liao, B. Xu, R. Yang, J. Hu, Y. Dai, and X. Qiu, Observation of topological nodal-line semimetal in $YbMnSb_2$ through optical spectroscopy, Phys. Rev. B **100**, 125136 (2019).

[20] J.-R. Soh, S. M. Tobin, H. Su, I. Zivkovic, B. Ouladdiaf, A. Stunault, J. A. Rodríguez-Velamazán, K. Beauvois, Y. Guo, and A. T. Boothroyd, Magnetic structure of the topological semimetal $YbMnSb_2$, Phys. Rev. B **104**, L161103 (2021).

[21] Y.-Y. Wang, S. Xu, L.-L. Sun, and T.-L. Xia, Quantum oscillations and coherent interlayer transport in a new topological Dirac semimetal candidate $YbMnSb_2$, Phys. Rev. Mater. **2**, 021201(R) (2018).

[22] Y. Pan, F.-R. Fan, X. Hong, B. He, C. Le, W. Schnelle, Y. He, K. Imasato, H. Borrmann, C. Hess, B. Büchner, Y. Sun, C. Fu, G. J. Snyder, and C. Felser, Thermoelectric properties of novel semimetals: A case study of $YbMnSb_2$, Adv. Mater. **33**, 2003168 (2021).

[23] K. Momma and F. Izumi, VESTA 3 for three-dimensional visualization of crystal, volumetric and morphology data, J. Appl. Crystallogr. **44**, 1272 (2011).

[24] K. C. Rule, R. A. Mole, and D. Yu, Which glue to choose? A neutron scattering study of various adhesive materials and their effect on background scattering, J. Appl. Crystallogr. **51**, 1766 (2018).

[25] See Supplemental Material at http://link.aps.org/supplemental/10.1103/PhysRevB.107.195146 for details of the sample characterization, the correction procedure for the inelastic neutron scattering data, and for additional figures showing fits to the data.

[26] E. Lelièvre-Berna, E. Bourgeat-Lami, Y. Gibert, N. Kernavanois, J. Locatelli, T. Mary, G. Pastrello, A. Petukhov, S. Pujol, R. Rouques, F. Thomas, M. Thomas, and F. Tasset, ILL polarised hot-neutron beam facility D3, Phys. B: Condens. Matter **356**, 141 (2005).

[27] B. Ouladdiaf, J. Archer, G. J. McIntyre, A. W. Hewat, D. Brau, and S. York, OrientExpress: A new system for Laue neutron diffraction, Phys. B: Condens. Matter **385-386**, 1052 (2006).

[28] A. T. Boothroyd, *Principles of Neutron Scattering from Condensed Matter* (Oxford University Press, New York, 2020).

[29] M. Kempa, B. Janousova, J. Saroun, P. Flores, M. Boehm, F. Demmel, and J. Kulda, The FlatCone multianalyzer setup for ILL's three-axis spectrometers, Phys. B: Condens. Matter **385-386**, 1080 (2006).

[30] S. Gull and J. Skilling, MEMSYS III Quantified Maximum Entropy Subroutine Library, 1989.

[31] A. J. Markvardsen, Polarised neutron diffraction measurements of $PrBa_2Cu_3O_{6+x}$ and the Bayesian statistical analysis of such data, Ph.D. thesis, University of Oxford, 2000.

[32] P. Steffens, nplot, matlab scripts for treatment of data from triple-axis spectrometers (2019), https://www.ill.eu/users/scientific-groups/spectroscopy/softwares, https://github.com/nplot/nplot.

[33] J. D. Hunter, Matplotlib: A 2D graphics environment, Comput. Sci. Eng. **9**, 90 (2007).

[34] C. R. Harris, K. J. Millman, S. J. van der Walt, R. Gommers, P. Virtanen, D. Cournapeau, E. Wieser, J. Taylor, S. Berg, N. J. Smith, R. Kern, M. Picus, S. Hoyer, M. H. van Kerkwijk, M. Brett, A. Haldane, J. F. del Río, M. Wiebe, P. Peterson, P. Gérard-Marchant *et al.*, Array programming with NumPy, Nature (London) **585**, 357 (2020).

[35] P. Virtanen, R. Gommers, T. E. Oliphant, M. Haberland, T. Reddy, D. Cournapeau, E. Burovski, P. Peterson, W. Weckesser, J. Bright, S. J. van der Walt, M. Brett, J. Wilson, K. J. Millman, N. Mayorov, A. R. J. Nelson, E. Jones, R. Kern, E. Larson, C. J. Carey *et al.*, SciPy 1.0: Fundamental algorithms for scientific computing in Python, Nat. Methods **17**, 261 (2020).

[36] J.-R. Soh, H. Jacobsen, B. Ouladdiaf, A. Ivanov, A. Piovano, T. Tejsner, Z. Feng, H. Wang, H. Su, Y. Guo, Y. Shi, and A. T. Boothroyd, Magnetic structure and excitations of the topological semimetal $YbMnBi_2$, Phys. Rev. B **100**, 144431 (2019).

[37] A. Sapkota, L. Classen, M. B. Stone, A. T. Savici, V. O. Garlea, A. Wang, J. M. Tranquada, C. Petrovic, and I. A.

Zaliznyak, Signatures of coupling between spin waves and Dirac fermions in $YbMnBi_2$, Phys. Rev. B **101**, 041111(R) (2020).

[38] S. Toth and B. Lake, Linear spin wave theory for single-Q incommensurate magnetic structures, J. Phys.: Condens. Matter **27**, 166002 (2015).

[39] X. Hu, A. Sapkota, Z. Hu, A. T. Savici, A. I. Kolesnikov, J. M. Tranquada, C. Petrovic, and I. A. Zaliznyak, Coupling of magnetism and Dirac fermions in $YbMnSb_2$, arXiv:2303.02587.

[40] J.-R. Soh, A. T. Boothroyd, A. Piovano, J. Sun, and S. M. Tobin, Magnon spectrum in a candidate topological semi-metal with magnetic order 2021, Institut Laue-Langevin (ILL), doi:10.5291/ILL-DATA.4-01-1684.

[41] J.-R. Soh, K. Beauvois, A. T. Boothroyd, J. A. Rodríguez-Velamázan, A. Stunault, and S. M. Tobin, Structural investigation of a possible magnetically-induced Weyl Semi-Metal $YbMnSb_2$, 2021, Institut Laue-Langevin (ILL), doi:10.5291/ILL-DATA.5-53-305.